Dalton Transactions

Accepted Manuscript

This is an *Accepted Manuscript*, which has been through the Royal Society of Chemistry peer review process and has been accepted for publication.

Accepted Manuscripts are published online shortly after acceptance, before technical editing, formatting and proof reading. Using this free service, authors can make their results available to the community, in citable form, before we publish the edited article. We will replace this *Accepted Manuscript* with the edited and formatted *Advance Article* as soon as it is available.

You can find more information about *Accepted Manuscripts* in the Information for Authors.

Please note that technical editing may introduce minor changes to the text and/or graphics, which may alter content. The journal's standard Terms & Conditions and the Ethical guidelines still apply. In no event shall the Royal Society of Chemistry be held responsible for any errors or omissions in this *Accepted Manuscript* or any consequences arising from the use of any information it contains.

ROYAL SOCIETY OF CHEMISTRY

www.rsc.org/dalton

Dalton Transactions

RSCPublishing

ARTICLE

Magnetically Stabilized $Fe_8(\mu_4\text{-}S)_6S_8$ Clusters in $Ba_6Fe_{25}S_{27}$

Cite this: DOI: 10.1039/xoxxoooooox

Timothy E. Stacey,[a b] Christopher K. H. Borg,[b] Peter J. Zavalij[b] and Efrain E. Rodriguez[b]

Received ooth January 2012,
Accepted ooth January 2012

DOI: 10.1039/xoxxoooooox

www.rsc.org/

We have prepared $Ba_6Fe_{25}S_{27}$, and studied its magnetic properties and electronic structure. Single crystal diffraction revealed a cubic phase (*Pm*-3*m*) with a = 10.2057(9) Å and Z = 1. Within the large cubic cell, tetrahedrally coordinated Fe atoms arrange into octonuclear $Fe_8(\mu_4\text{-}S)_6(S_8)$ clusters, which can be described as a cube of Fe atoms with six face-capping and eight terminal S atoms. SQUID magnetometry measurements reveal an antiferromagnetic transition at 25 K and anomalous high-temperature dependence of magnetic susceptibility that is non-Curie like—two magnetic signatures which mimic behavior seen in the parent phases of Fe-based superconductors. Using a combined DFT and molecular orbital based approach, we provide an interpretation of the bonding and stability within $Ba_6M_{25}S_{27}$ (M=Fe, Co, Ni) and related M_9S_8 phases. Through a σ-bonding molecular orbital model of the transition metal coordination environments, we illustrate how the local stability can be enhanced through addition of Ba. In addition, we perform spin-polarized DFT calculations on $Ba_6Fe_{25}S_{27}$ to determine the effect of adopting an antiferromagnetic spin state on its electronic structure. By studying the magnetic properties from an empirical and computational perspective, we hope to elucidate what aspects of the magnetic structure are significant to bonding.

Introduction

Cluster-forming iron sulfides have long interested chemists for their structural diversity and bioinorganic functions. For example, nonheme iron sulfur proteins can be found in bacterial ferredoxins, which can contain the cubane-type Fe_4S_4 clusters involved in anaerobic metabolism.[1, 2] Efforts to synthetically reproduce iron sulfide clusters have therefore been pursued to better understand their bonding and electron transfer properties.[3-7]

Although a plethora of cluster structures and sizes can be constructed for edge-sharing tetrahedra, the rhombic dodecahedron with the formula M_8L_{14} is one of the most commonly encountered in metal chalcogenides.[8] These large metal sulfide clusters can be reproduced synthetically either in the solid state or in molecular complexes. Lower and Dahl were the first to prepare a complex with this rhombic unit in $Ni_8(\mu_4\text{-}PPh)_6(CO)_8$,[9] where the nickel atoms form the corners of a cube, the μ_4-phenyl phosphines cap the faces of the cube, and the carbonyls are the terminal ligands (Figure 1a). The work on the Ni complexes was largely extended by Fenske *et al.*,[10-12] while Christou *et al.* explored the Co-analogues in anionic species such as $[Co_8(\mu_4\text{-}S)_6(SPh)_8]^{4-}$.[13, 14] Phol and Saak were able to successfully reproduce the iron clusters in species such as $[Fe_8(\mu_4\text{-}S)_6I_8]^{4-}$.[15-17]

The rhombic dodecahedral cluster was first observed, however, not in molecular complexes but within the mineral known as pentlandite.[18] The archetypical stoichiometry of pentlandite is Co_9S_8, and just as observed in $Ni_8(\mu_4\text{-}PPh)_6(CO)_8$, part of the pentlandite crystal structure adopts a rhombic dodecahedral cluster composed of transition metal and S atoms (Figure 1b). The terminal CO and face-capping PPh ligands of the molecular complex are replaced by S anions, and this arrangement around the Co_8 cube completes a tetrahedral coordination for each of the Co atoms. Thus, the rhombic dodecahedron of pentlandite can be dually thought of as a packing of eight CoS_4 units. Within the unit cell, the sulfur atoms of the $Co_8(\mu_4\text{-}S)_6S_8$ cluster are also shared by CoS_6 octahedra (Figure 1b).

[a] Department of Physics, University of Maryland, College Park, MD 20742.
[b] Department of Chemistry and Biochemistry, University of Maryland, College Park, MD 20742. Email: efrain@umd.edu

†Electronic Supplementary Information (ESI) available: The crystallographic information file, Hückel parameters, and details of DFT calculations.

Dalton Transactions Accepted Manuscript

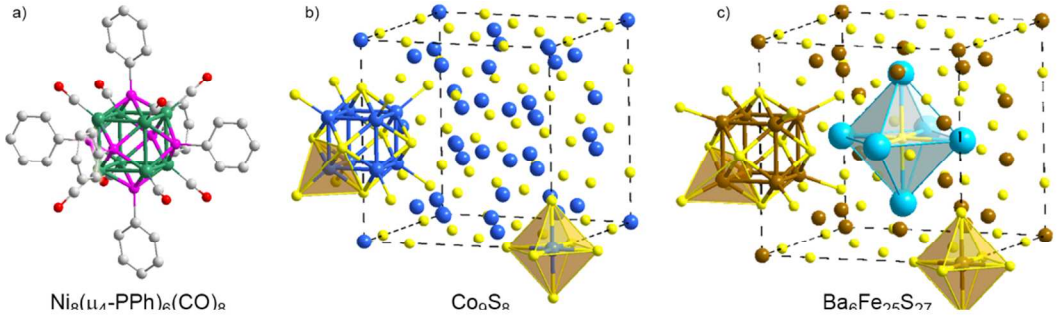

Figure 1. (a) $Ni_8(\mu_4\text{-}PPh)_6(CO)_8$, the first M_8-octonuclear complex with the rhombic dodecahedral structure prepared by Lower and Dahl (Ni=green, P=purple). (b) The mineral pentlandite, Co_9S_8, with the rhombic dodecahedral motif (Co=blue, S=yellow), and (c) the title compound $Ba_6Fe_{25}S_{27}$ with similar structural motifs as in pentlandite (Fe=brown, S=yellow). Octahedral coordination for the transition metal is also found in the latter two.

Related extended solids of recent interest include the iron-based superconductors, where a 2D square array of Fe centres are capped by μ_4-*X* ligands for *X* = S, Se, Te, P, or As.[19-21] Also common to all phases is the antiferromagnetic ground state that must be suppressed either through pressure (physical or chemical) or electron/hole doping in order to induce superconductivity.[22-28]

In light of the plethora of superconducting pnictides and chalcogenides containing tetrahedral Fe^{2+} centers,[29-33] the search for new phases containing such species but with different iron-connectivity such as clusters (0D units) could lead to interesting discoveries. Indeed, superconductivity was found for the first time in metal sulfides in the so-called Chevrel phases, which contain Mo_6Q_8 clusters for Q = S, Se, or Te.[34, 35] Reminiscent of Re_6Q_8 cluster chemistry,[36, 37] the Chevrel phases also display structural chemistry intermediate between the molecular and solid-state, where both electron count per Mo_6 octahedron and intercluster interactions play critical roles in its stabilization, redox chemistry, and superconducting properties.[38, 39]

In this Article, we report the structure and synthesis of a novel phase, $Ba_6Fe_{25}S_{27}$, which contains $Fe_8(\mu_4\text{-}S)_6S_8$ clusters similar to those found in the molecular complexes and naturally occurring minerals. Although approximately 20 different phases in the Ba-Fe-S ternary system are known, this is the only one containing the octonuclear cluster.[40-44] In contrast, only a few ternary sulfides containing Ba are known for Co and Ni, yet the isostructural $Ba_6Co_{25}S_{27}$ and $Ba_6Ni_{25}S_{27}$ phases had been found earlier by DiSalvo *et al.* [45, 46] The stability of these phases contrast with the observed M_9S_8 phases. Pentlandite-like Fe_9S_8 and Ni_9S_8 are not observed to form, but the inclusion of Ba cations stabilizes the rhombic dodecahedral units found in Co_9S_8.

To explore the mechanisms behind this observed structural chemistry, we characterize the $Ba_6Fe_{25}S_{27}$ phase through two means: SQUID magnetometry and electronic structure analysis. By constructing a molecular orbital (MO) bonding model of the metal sites' local coordination within the $Ba_6M_{25}S_{27}$ (M=Fe, Co, Ni) and related M_9S_8 phases, we are able to assess which bonding interactions are central to the extended solid stability. Our model is based on Hückel parameters that are calibrated against density functional theory (DFT). This approach yields both the accuracy of DFT techniques and the transparency of a Hückel model. We finish by assessing the role of magnetism in stabilizing $Ba_6Fe_{25}S_{27}$ with magnetic susceptibility measurements and spin-polarized DFT.

Experimental and computational methods

Sample preparation: $Ba_6Fe_{25}S_{27}$ was first observed in powder X-ray diffraction patterns from reactions of BaS (99.9 %, Sigma Aldrich), FeS (Fischer), and Fe metal (J.T. Baker) in stoichiometric mixtures prepared in quartz ampoules *in vacuo* at 1000 °C. The powder pattern readily indexed to a cubic space group with lattice constant *a* = 10.2427(3) Å at room temperature. Other impurities were found such as FeS (troilite) and $BaFe_2S_3$, a polymeric compound.[44]

For single crystal growth, powder mixtures of BaS:Fe:S (99.5%, Sigma Aldrich) in a 6:25:21 ratio were ground, pelletized, and placed in graphite crucibles. The crucible was placed in a fused quartz ampoule and torch sealed under vacuum (approximately 30 mTorr). The ampoule with sample was heated in a three-zone tube furnace up to 400 °C at 90 °C/hr and held there for 4 hours. The sample was then heated at 90 °C/hr up to 950 °C and held there for 72 hours. Afterwards, the sample was slow cooled at a rate of 2 °C/hr down to 750 °C and then more rapidly cooled to room temperature at a rate of 90 °C/hr.

From the growth conditions, a spherical dull grey pellet was broken open revealing multiple dark lustrous crystals with cubic crystal habits. Powder X-ray diffraction patterns of a ground sample revealed 82 wt. % $Ba_6Fe_{25}S_{27}$, 4 wt. % $Ba_2Fe_4S_5$, 11 wt. % $BaFe_2S_3$, and 3 wt. % FeS (troilite) from Rietveld analysis.

X-ray structural determination: Diffraction data were collected on a black prism-like crystal of approximate dimensions 0.03 mm x 0.11 mm x 0.18 mm. Mounted on a

Dalton Transactions Accepted Manuscript

glass fiber, the crystal was measured at 150 K using the Bruker APEX-II CCD system.[47] The structure was solved with direct methods and refined using the Bruker SHELXTL Software Package.[48] The crystal was found to belong to a cubic system. Further experimental details are included in Table 1.

Table I. Single-crystal X-ray diffraction data for $Ba_6Fe_{25}S_{27}$.

Space group	*Pm*-3*m* (No. 221)
a (Å)	10.2057(9)
Crystal system	Cubic
Volume (Å^3)	1063.0(3)
Z	1
Formula weight	3085.91
Calculated density (g/cm^3)	4.821
λ, Mo Kα (Å)	0.71073
Monochromator	Graphite
no. of reflections collected	17812
no. of independent reflections	412
Absorption coefficient (mm^{-1})	15.006
F(000)	1418
R_1, wR_2 (%)	1.36, 3.95

$$R_1 = \sum ||F_o| - |F_c|| / \sum |F_o|$$

$$wR_2 = \left\{ \sum [w(F_o^2 - F_c^2)^2] / [w(F_o^2)^2] \right\}^{1/2}$$

Magnetic susceptibility measurements: For the magnetization measurements, approximately 15 crystals were selected under the microscope totaling 1.5(1) mg. The crystals were checked by X-ray diffraction for phase purity. A Magnetic Properties Measurement System (MPMS XL-7) from Quantum Design was utilized for carrying out the SQUID magnetization measurements as a function of temperature. The crystals were enclosed in a gelatin capsule in a clear plastic straw and zero-field cooled (ZFC) down to 1.8 K. A field of 1000 Oe was applied (due to small sample size) and the magnetization was measured upon warming to 300 K.

First-principles calculations: Density Functional Theory (DFT) with Generalized Gradient Approximation[49] (GGA) were employed using the Vienna Ab-initio Software Package (VASP)[50-53] and Projector Augmented Wave[54, 55] (PAW) potentials for geometrical optimizations of Co_9S_8, Fe_9S_8, and Ni_9S_8 and calculation of their density of states (DOS) distributions and band structures. Fe_9S_8 and Ni_9S_8 are hypothetical phases, which necessitated the use of geometrical optimization to obtain reasonable models. The geometrical results are reported in the Supporting Information. GGA-DFT calculations were also used to calculate the DOS distribution and band structures of $Ba_6Fe_{25}S_{27}$, $Ba_6Co_{25}S_{27}$, and $Ba_6Ni_{25}S_{27}$, using experimentally reported coordinates within this article and previous reports.[45, 46] In order to model the magnetic properties within $Ba_6M_{25}S_{27}$ (M=Fe, Co, Ni) phases, spin-polarized calculations were used. In accordance to the VASP manual, magnetic moments of each metal center were each given an abnormally high magnetic moment and then allowed to converge on a stable state.

Because of the localized nature of transition metal d-orbitals within chalcogenide phases, DFT+U methods[56] were applied to achieve more accurate representation of the electron correlation. Within our calculations, we employed the technique of Dudarev et al.,[57] where the U and J terms are taken together as a single parameter (U-J). We applied a U-J term value of 4.5 eV for each phase. Because our investigations are largely based around a molecular orbital (MO) bonding picture, the individualized fitting of U_{eff} terms to specific phases was not crucial.

Our investigations into the effect of local bonding on phase stability in this Article were conducted by constructing simple Hückel-based[58-61] molecular orbital (MO) models. All Hückel calculations were performed using the YaeHMOP software[62] with the Wolfsberg-Helmholtz approximation[63] and the correction for counterintuitive orbital mixing turned off.[64] Within the Hückel model, each orbital was modeled with two types of parameters. The H_{ii} parameter makes up the ionization potential of the orbital, and also represents the diagonal terms of the Hamiltonian matrix. The ζ parameter represents the decay of the wavefunction from the nucleus, which can also be interpreted as a shielding coefficient. For each atom, s- and p-orbitals were modeled with a single-ζ value while d-orbitals were modeled with a double-ζ basis. Implementing a double-ζ basis for the d-orbitals is a standard practice[75,77-80] that enhances the ability of the d-orbital to model contracted nonbonding-like behaviour and more diffuse characteristics emanating from bonding.

To accurately represent the bonding within the phases studied, Hückel parameters were optimized to match the DFT result with a least squared fitting of the calculated band structure and DOS distribution. This fitting was made possible through the *eHtuner* program.[65] Each fitting was performed up to 1 eV above the DFT calculated Fermi energy for each phase.

Further details of these calculations, including energy cutoffs, k-point meshes, and Hückel parameters are supplied in the Supporting Information.

Results and discussion

Structural details: Structural parameters from the single crystal data are listed in Table II and relevant interatomic distances in Table III. As can be seen from Table II, there are two unique Fe sites and four S^{2-} positions. The iron site located at general Wyckoff position 24m comprises the rhombic cluster, while the iron located at special position 1a, the octahedral site. The Fe-Fe bond distances are split into two sets due to a tetragonal-type distortion on the Fe_8-cluster.

It is instructive to compare the pentlandite structure[18] with that of $Ba_6Fe_{25}S_{27}$, which we compare in Figure 2. The combination of the Co_8S_{14} clusters and octahdedral units

Dalton Transactions Accepted Manuscript

forms the total pentlandite motif, and these units pack in a rock-salt type fashion to fill the unit cell (Figure 2a). The isostructural $Ba_6Co_{25}S_{27}$ and $Ba_6Ni_{25}S_{27}$ phases discovered

Table II. Structural parameters from single crystal data for $Ba_6Fe_{25}S_{27}$.

atom	Site	x	y	Z	U_{equiv} ($Å^3$)*
Ba(1)	6f	0.5	0.5	0.19719(3)	0.0063(1)
Fe(1)	24m	0.13324(3)	0.36384(4)	0.13324(3)	0.0080(1)
Fe(2)	1a	0.0	0.0	0.0	0.0084(4)
S(1)	1b	0.5	0.5	0.5	0.0060(5)
S(2)	6e	0.0	0.24009(13)	0.0	0.0064(2)
S(3)	8g	0.28140(7)	0.28140(7)	0.28140(7)	0.0064(2)
S(4)	12h	0.0	0.5	0.25330(9)	0.0061(2)

*Isotropic atomic displacement parameters U_{equiv} are defined as one-third of the trace of the orthogonalized U_{ij} matrix.

Table III. Select interatomic distances (Å) and angles (°) for $Ba_6Fe_{25}S_{27}$.

Fe1—S2	2.3007(9)	S3—Fe1—S4	2 × 105.06(3)
Fe1—S3	2.2980(8)	S4—Fe1—S4	105.38(3)
Fe1—S4	2 × 2.2981(6)	S3—Fe1—S2	125.23(4)
Fe2—S2	6 × 2.4503(13)	S4—Fe1—S2	2 × 107.30(2)
Fe1—Fe1	2 × 2.7196(6)	S2—Fe2—S2	90.0, 180.0
Fe1—Fe1	2.7793(9)	Ba1—S1	3.0904(4)
		Ba1—S3	4 × 3.2700(8)
		Ba1—S4	4 × 3.2232(8)

by DiSalvo *et al*. [45, 46] preserve large fragments of the pentlandite atomic arrangement. These compounds assume the djerfisherite-type structure,[66, 67] in which a matrix of the pentlandite structure is implanted with pockets of ionic clusters (Figure 2b). In the case of $Ba_6Co_{25}S_{27}$ and $Ba_6Ni_{25}S_{27}$, the inclusion of cationic Ba_6S octahedra as an additional component to the pentlandite structure interrupts the rock-salt ordering. This arrangement of the octonuclear M_8S_{14} clusters, MS_6 octahedra, and Ba_6S octahedra is analogous to the ordering seen in perovskite type structures (Figure 2b).

Within $Ba_6Fe_{25}S_{27}$, the $Fe_8(\mu_4\text{-}S)_6S_8$ clusters share some of their S^{2-} anions either with other rhombic units or FeS_6 octahedra. The face-capping μ_4-S is now split into two unique sites, where one (site 12h, Table II) remains free as in the ligands of the molecular complexes, while the other (site 6e) bridges to the neighboring FeS_6 octahedra. The terminal S^{2-} ligands (site 8g) are now shared among three rhombic units instead of being free as in the molecular complexes. The last sulfide (site 1b) is located at the center of the cube and coordinates to six Ba^{2+} cations.

Theoretical Discussion: Our synthesis of $Ba_6Fe_{25}S_{27}$ has focused our attention on solid state compounds which contain the $M_8(\mu_4\text{-}S)_6S_8$ cluster. As we have noted, ternary 6:25:27 phases which contain the $M_8(\mu_4\text{-}S)_6S_8$ motif are Fe, Co, and Ni based, while the M_9S_8 phase is stable for a limited range of transition metal substitution. The allowable

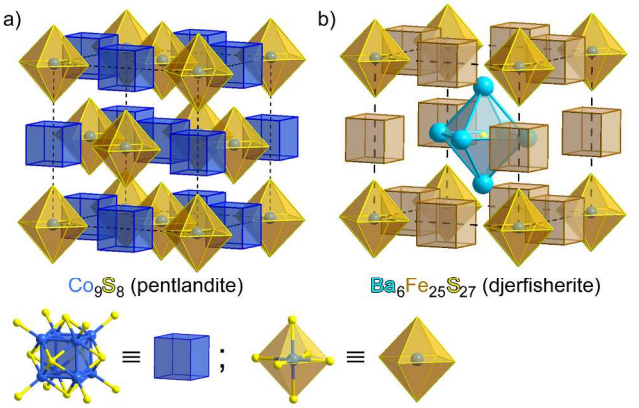

Figure 2. (a) The pentlandite structure, Co_9S_8. In pentlandite, the $M(\mu_4\text{-}S)_6S_8$ motif and the MS_6 octahedra are packed in a face-centered cubic array for a rock-salt superstructure. (b) In the djerfisherite-type structure, exhibited by $Ba_6Co_{25}S_{27}$, the FCC packing of the two motifs is disrupted by the central $(SBa_6)^{10+}$ octahedra, leading to a perovskite-like superstructure.

substitution for a stable pentlandite phase centers around having a stoichiometry that is isoelectronic with Co_9S_8 (d-electron count of ~58-59). The end members of the series, Fe_9S_8 and Ni_9S_8, are not observed to form from conventional solid state synthesis.[68, 69]

Since the ternary phases exist for Ni and Fe, while the simple binaries do not, this raises a question of how incorporating ionic species such as $(SBa_6)^{10+}$ can stabilize the rhombohedral cluster. To understand the structural chemistry of the 6:25:27 phases, we begin by performing an electronic structure analysis of the pentlandite phase. The binary compound permits us to decouple the contributing roles of the pentlandite motif and the addition of Ba cations to produce a stable ternary phase.

The electronic structure of pentlandite Co_9S_8: The electronic structure of the rhombohedral $M_8(\mu_4\text{-}X)_6Y_8$ cluster has been explored by a number of previous studies.[70-73] Through extended Hückel and self-consistent field multiple scattering calculations, Furet et al. found a large range in valence electron count for the various $M_8(\mu_4\text{-}X)_6Y_8$ molecular complexes—from 99 to 120 electrons—due to the flexibility of $M_8(\mu_4\text{-}S)_6Y_8$ π-type bonding and M-M bonding.[70] From the solid state perspective, the bonding of this cluster in Co_9S_8 was originally explored by Burdett and Miller using extended Hückel theory.[71] It was determined that the Co-S bonding within the structure has a very strong role in mediating the stability of the rhombohedral cluster, and that the electron count of the phase aligns with keeping Co-S antibonding levels unoccupied. The multiple scattering method was also employed in a study by Hoffman et al. to characterize clusters with a rhombohedral $Co_8(\mu_4\text{-}S)_6$ core.[72] Finally, the link between electron count and stability of Co_9S_8 has also been explored by DFT techniques—Chauke et al. determined that the heat of formation of both Co_9S_8 and

Dalton Transactions Accepted Manuscript

$Fe_5Ni_4S_8$ is correlated with a pseudogap separating bonding and antibonding states.[73]

To begin our bonding investigation, we start at a similar point to Chauke et al,[73] which will lay the foundation for a new, local coordination based model. In Figure 3, we show the result from our DFT calculations in the form of DOS distribution for Co_9S_8, and hypothetical examples of Fe_9S_8 and Ni_9S_8. The projected DOS (pDOS) distribution of the transition metal (M) d-states are plotted in blue stripes, and the pDOS of the S p-states are outlined in orange. The DOS distribution is plotted from -15 to -3 eV, focusing on the valence bands. Core-like states from the S 3s orbitals reside around -20 eV with very little broadening.

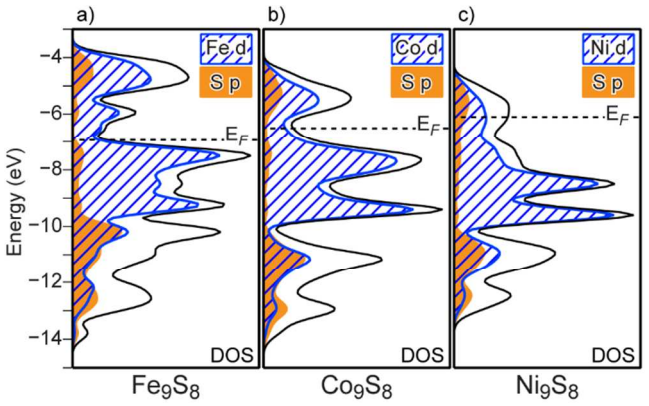

Figure 3. DOS distributions of M_9S_8 (M=Fe,Co,Ni), calculated from GGA-DFT. The total DOS curve is outlined in black, projected DOS distributions for the M d-states are filled in blue stripes, and S p-states are filled in orange. The black dashed line marks the Fermi energy for each distribution.

Starting with Co_9S_8 (Fig. 3b), there appear to be three unique sets of states. The low end of the energy spectrum is made up of occupied states with both Co d- and S p-character, suggestive of bonding interactions. At the middle of the spectrum, few S p-states are present and the DOS distribution is largely made up of sharp peaks from the Co d-states—these appear to have more nonbonding character. Finally, above the Fermi level at 6.50 eV, the S p-states resume their appearance alongside Co d-states to produce a regime of antibonding states. The Fermi level, within this description, is nestled between the antibonding and nonbonding states, just as expected for the HOMO-LUMO gap in a molecular complex. From this qualitative assessment, our theoretical result align well those of Burdett and Miller, and Chauke et. al.[71, 73]

In comparing the Co_9S_8 picture to the Fe and Ni analogues, we can see that the Fe and Ni DOS distributions are very similar. All three distributions show distinct divisions into three regions, and the S p-states only express their character in the highest and lowest regions of the curve. In the case of Fe_9S_8 DOS, the pseudogap appears less smooth in comparison to Co_9S_8. The central block of Fe d-states shifts higher in energy while the Fermi energy sinks lower in comparison to Co_9S_8, causing the two to almost intersect. The Fermi energy of Ni_9S_8, on the other hand, rises in energy, above the perceived pseudogap in its distribution. The increasing number of electrons with atomic number explains the variation of the Fermi level for the three DOS distributions. The spread of the distribution also changes, affecting the appearance of the pseudogap.

By analyzing these DOS distributions, we have observed hints of molecular bonding within the pentlandite phase. To tease these bonding interactions out from the reciprocal space perspective, we have developed a DFT-calibrated Hückel model that will further illustrate these ideas.

Local coordination model of Co_9S_8: Hückel theory, originally developed to characterize conjugated hydrocarbon species,[58-61] has been expanded over time to understand a wide range of chemical bonding behavior, particularly within inorganic complexes. One landmark extension of this theory is to transition metal-ligand interactions, explored by Burdett through use of the angular overlap approach.[74] Hückel calculations have also proven vital to understanding solid state bonding, providing transparency to band structures of extended solids.[75-77]

Most recently, DFT-calibrated Hückel calculations have revealed a strong relationship between the resulting molecular orbital (MO) diagrams of local coordination environments and the extended solids within which they are embedded.[78-80] In the following sections, we will take a similar approach to develop σ-bonding MO models to explain the chemistry of octonuclear cluster containing phases. Within our model, we only consider the local coordination of the metal sites as Crystal Hamilton Overlap Populations (COHP)[81] calculations we have performed indicate that M-S interactions far eclipsing the strength of M-M interactions.

We begin by obtaining a Hückel parameter set which is reflective of the DFT-result. By refining the parameter set using *eHtuner*,[65] band structures and DOS distributions from Hückel theory were fit against those calculated from GGA-DFT. The resulting parameter sets are given in the Supplementary Information. The root mean squared deviation between the Hückel and DFT calculated band structures for all parameterizations in this paper do not exceed 0.15 eV up to 1 eV past the Fermi energy. In Figure 4a, we present the DOS distribution of Co_9S_8 calculated from DFT-calibrated Hückel theory. Just as in the DFT result, the Co_9S_8 DOS distribution calculated from Hückel theory (Figure 4a) exhibits a distinct pseudogap that aligns with the Fermi level.

Using the DFT-calibrated Hückel parameters, we have constructed a model for the bonding within each of the coordination environments of Co. These calculations employ a basis set using metal 4s, 4p, and 3d orbitals and S 3s and 3p orbitals. For each MO diagram, we construct σ-type bonding orbitals for each adjoining ligand (a linear combination of S s- and p-orbitals), which point towards the metal atom. These orbitals combine to make symmetry-adapted linear combinations (SALCs), which then can form molecular orbitals with the central metal states.

Dalton Transactions Accepted Manuscript

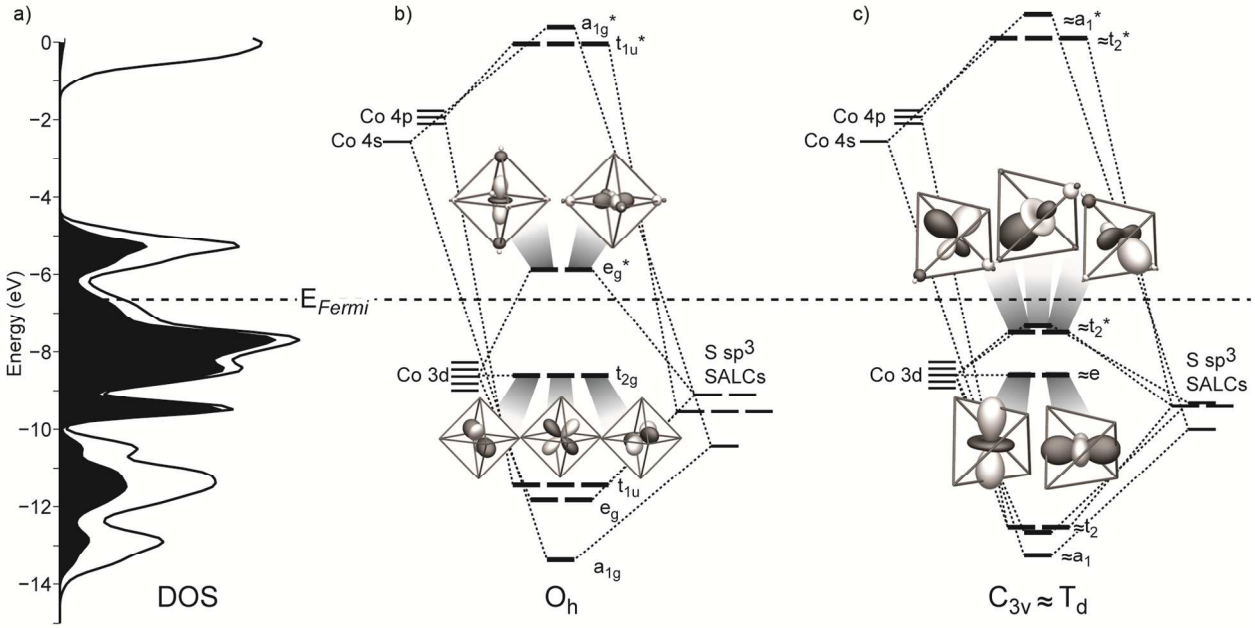

Figure 4. a) DOS distribution of Co_9S_8, calculated from DFT-calibrated Hückel theory. Co d-states are filled in black, and the Fermi level is marked in a dashed black line. b) MO diagrams for the octahedral CoS_6 unit and c) tetrahedral CoS_4 unit in Co_9S_8, calculated from a σ-bonding model based on DFT-calibrated Hückel parameters. Spatial representations of the valence MOs are plotted above and below the corresponding energy levels.

MO OF THE O_H CoS_6 COORDINATION: The resulting MO diagram from the octahedral CoS_6 unit is depicted in Figure 4b. The octahedral coordination environment assumes perfect O_h symmetry with no distortions. The available coordinating σ-bonding ligand orbitals form a_{1g}, t_{1u} and e_g sets of SALCs, which bond with the metal center to produce three bonding and antibonding sets of states. The set of t_{2g} orbitals come directly from the metal ion, forming a nonbonding orbital set at -8.60 eV. Most of the bonding and antibonding states are grouped tightly in the distribution, but the t_{2g} and e_g* states are set apart in the continuum of states.

By plotting the MO diagram for the octahedral cluster alongside the DFT-calibrated Hückel DOS distribution, we can begin to see similarities between the two. Many of the peaks within the DOS distribution parallel where the states in the MO diagram are focused. Notably, the energies of the e_g* states in the MO diagram and the peak above the pseudogap in the DOS are highly consistent. Just as the pseudogap is centered on the Fermi level, the e_g* and t_{2g} states also arrange above and below the Fermi energy. The Fermi level cuts through the HOMO-LUMO gap, right below the e_g* states. The six bonding orbitals form a_{1g}, t_{1u}, and e_g interactions and the additional t_{2g} states sit below the Fermi energy, making for an occupied nine states and satisfying the oft-cited 18 electron rule. In Figure 4b, we also show the spatial distributions for the t_{2g} and e_g* orbitals of the octahedral cluster, demonstrating their respective nonbonding and antibonding arrangements.

MO OF THE ≈T_D CoS_4 COORDINATION: The tetrahedral CoS_4 unit within the pentlandite structure takes on a slight distortion, reducing the symmetry from T_d to C_{3v}. The distortion, however, is small enough that we can view the resulting MO diagram (Figure 4c) from the perspective of T_d symmetry. In T_d symmetry, the σ-bonding ligands adopt two sets of SALCs—one a_1 state and the triply degenerate t_2 states. Bonding with the low energy a_1 SALC forms one low and one high energy MO. The ~t_2 SALC bonds with the Co d- and p-orbitals to form three sets of MO's. Finally, two Co d-orbitals remain unbonded, creating the nonbonding *e* set.

The Fermi energy of Co_9S_8 lands right above the midrange energy states from the tetrahedral cluster, and well before the high lying antibonding states of the cluster. Again, nine states from the tetrahedral cluster arrange below the Fermi energy creating an electron count of 18. Although less cited, other inorganic complexes in tetrahedral coordination can obey the 18 electron rule.[82] The difference in energy between the *e* and t_2* states in a T_d-symmetry complex is often small, thus enhancing the preference for the t_2* set to be filled and act as the HOMO. The inclusion of π interactions can also potentially further enhance the bonding character of the t_2* set.

The spatial distributions of the resulting molecular orbitals in the CoS_4 unit bear slight differences to the typical MO set expected for T_d symmetry (Figure 4c). If these states are manipulated by taking linear combinations of the resulting wavefunctions, however, the result can achieve a greater correspondence to what is typically observed as the t_2* set in tetrahedral complexes. Although some antibonding interaction is observed in this t_2* set, the more dominant features involve large metal d-lobes which point away from antibonding interactions (Figure 4c). The lower lying *e* states are essentially nonbonding in character.

From our evaluation of Co_9S_8 with a first coordination sphere approach, we see that the fortuitous electron count of

Dalton Transactions Accepted Manuscript

the compound satisfies the population of bonding and nonbonding orbitals within each cluster unit. While this satisfaction of the 18-electron rule for both coordination environments helps explain the stability of Co_9S_8, it can also inform our understanding of the instabilities for alternative stoichiometries.

Local model applied to hypothetical M_9S_8 phases: As we saw previously in the DOS distributions of Figure 4, the match between the Fermi energy and the pseudogap is very clear for Co_9S_8, but more states tend to spill around the Fermi energy for Fe_9S_8 and Ni_9S_8. We can apply the cluster MO model to Fe_9S_8 and Ni_9S_8 to see if we can understand the source of these differences in the local electronic structure. In Figure 5a-c, we show the MO diagrams for the octahedral unit within Fe_9S_8, Co_9S_8, and Ni_9S_8.

For each MO diagram, the Fermi energy from the extended solid calculation is superimposed. All three phases retain a similar distribution of states, but now their relative positioning to the Fermi energy has changed. From left to right, the Fermi energy increases, which can be explained by the increase in overall electron count with increasing transition metal atomic number. In the case of Fe_9S_8 and Co_9S_8, the t_{2g} and e_g* energy levels flank the Fermi energy, filling the nonbonding t_{2g} state and leaving the antibonding state unfilled. Ni_9S_8, on the other hand, has a Fermi energy which exceeds the energy of the e_g* level, meaning that states with strong antibonding character are now filled.

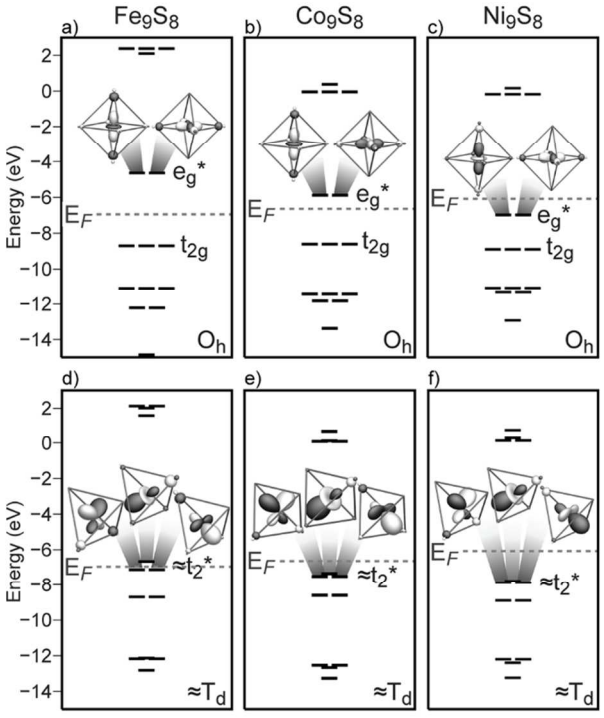

Figure 5. MO diagrams of the a-c) MS_6 and d-f) MS_4 units within Fe_9S_8, Co_9S_8, and Ni_9S_8. The corresponding M_9S_8 Fermi level is derived from an extended solid DFT-calibrated Hückel calculation and superimposed within each MO diagram. Selected spatial distributions of valence MOs are additionally plotted.

The shift of the Fermi energy has an opposing effect on the stability of the tetrahedral unit. Starting from the right in Figure 5f, the Fermi level locates above the bonding and nonbonding states of the tetrahedral cluster in Ni_9S_8 without intruding into antibonding states. At Fe_9S_8, the Fermi level finally intersects with these nonbonding states, causing some of the states to exceed the Fermi level. This intersection in the FeS_4 MO diagram is suggestive of the tetrahedral cluster losing its ability to retain a stable 18 electron count.

Incorporation of $(SBa_6)^{10+}$ units: So far we have observed that our MO models begin to pinpoint sources of electronic stability and instability among the local metal coordination in the pentlandite structure. Within the $Ba_6Fe_{25}S_{27}$ compound that we synthesized, and the other 6:25:27 phases, a similar network of octahedral and tetrahedral units make up a large portion of the structure. Can we apply the same MO model to the 6:25:27 phases? To answer this question, we must determine how much the $(SBa_6)^{10+}$ clusters perturb the covalent bonding within the original pentlandite structural motif.

The charge distribution of $Ba_6Fe_{25}S_{27}$ provides insight into how the $(SBa_6)^{10+}$ octahedra affect the Fe-S bonding in the pentlandite structure. In Figure 6, we plot an electron density isosurface for the unit cell of $Ba_6Fe_{25}S_{27}$. The isosurface is plotted in gray, and slices through the isosurface are plotted in a color map to indicate the internal gradient of electron density at the slice. Within this representation, we focus on the gray isosurface surrounding the atoms. The pentlandite matrix, composed of Fe and S atoms, fills a majority of the unit cell and surrounds the ionic $(SBa_6)^{10+}$ unit. Electron density clouds stretch along the sulfur-iron bonds to produce a highly directed surface with maximum volume around the S and Fe atoms.

In order to see the distribution of electrons directly resulting from the $(SBa_6)^{10+}$ units, we isolate the central cluster on the right side of Figure 6. The density isosurface is cut at planes which surround $(SBa_6)^{10+}$.

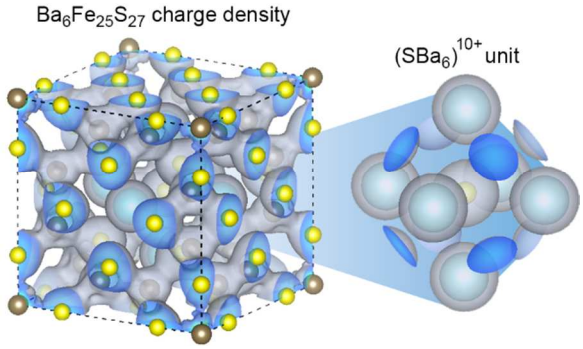

Figure 6. Electron density distribution of the $Ba_6Fe_{25}S_{27}$ unit cell (left) and the $(SBa_6)^{10+}$ unit (right) embedded within the structure. The outer isosurface of the electron density is plotted in grey, while the sections through the electron density surface are plotted in dark blue. Ba, Fe, and S atoms are represented in light blue, brown, and yellow, respectively. Electron density appears around the Ba atoms due to the use of a pseudopotential with semicore electrons.

Dalton Transactions Accepted Manuscript

Each atom within the isolated $(SBa_6)^{10+}$ unit is surrounded by an isotropic distribution of electron density, indicative of purely ionic type bonding in this region of the structure.

THE MO PERSPECTIVE OF THE 6:25:27 PHASES: Due to the apparent lack of covalent interaction between the pentlandite matrix and the $(SBa_6)^{10+}$ unit, we can reuse our previous approach to characterize the electronic structure of $Ba_6Fe_{25}S_{27}$, $Ba_6Co_{25}S_{27}$ and $Ba_6Ni_{25}S_{27}$. For each 6:25:27 phase, we again create an MO model from DFT-parameterized Hückel theory for the tetrahedral and octahedral clusters.

Within each MO diagram, we again superimpose the Fermi energy to indicate the highest filled energy levels within the distribution. Unlike in the pentlandite phases, the Fermi level does not have a linear dependence on the transition metal atomic number of the 6:25:27 phases. This lack of a direct trend can possibly be affected by a number of differences between the three phases. For instance, the variance in geometry between the three phases is also independent of electron count—the Fe and Ni based compounds exhibit shorter M-S and M-M bond distances and smaller unit cells in comparison to the Co case.

MS_6 units within the 6:25:27 phases exhibit MO diagrams (Figures 7a-c) very similar to what is observed for pentlandite, with slight variation. In the case of $Ba_6Fe_{25}S_{27}$ and $Ba_6Co_{25}S_{27}$, the t_{2g} and e_g* energy levels continue their positioning above and below the Fermi energy. We observe a signficant change, however, at the MO diagram for the NiS_6 unit within $Ba_6Ni_{25}S_{27}$ (Figure 7c). The e_g* set is now slightly raised over the Fermi level of $Ba_6Ni_{25}S_{27}$, indicating a depopulation of the antibonding levels of the NiS_6 unit. Overall, the entire distribution of states of the NiS_6 unit has spread out significantly compared to the hypothetical Ni_9S_8 phase.

The distribution of states for the MS_4 unit in the 6:25:27 phases (Figures 7d-f) bear less one-to-one correspondence to the pentlandite T_d MO diagrams, partly due to continued distortion of the tetrahedral coordination environment of the metal atoms. The previously established framework is still a useful gauge of local bonding stability. The tetrahedral cluster within $Ba_6Co_{25}S_{27}$ and $Ba_6Ni_{25}S_{27}$ exhibits an MO diagram with nine states below the Fermi level, satisfying an 18 electron count. This set of states includes the slightly antibonding t_2* states. From the plotted molecular orbitals, we can see that only slight antibonding character continues to persist at this energy level—large lobes of the central metal ion point away from antibonding interactions, while smaller lobes point towards ligands with a significantly reduced projection.

The $Ba_6Fe_{25}S_{27}$ T_d MO diagram tells a different story. As observed before in the pentlandite model, the Fe based compound has a lower Fermi energy than in the Co and Ni cases. Originally, this seemed like a destabilizing characteristic in pentlandite-like Fe_9S_8, as the cluster was not able to satisfy an electron count of 18 as in Co_9S_8. Within $Ba_6Fe_{25}S_{27}$, however, we observe a new twist: the T_d electronic configuration pushes the orbitals that exhibit slight antibonding character further above the Fermi energy. Thus, instead of trying to satisfy an 18-electron count rule, the

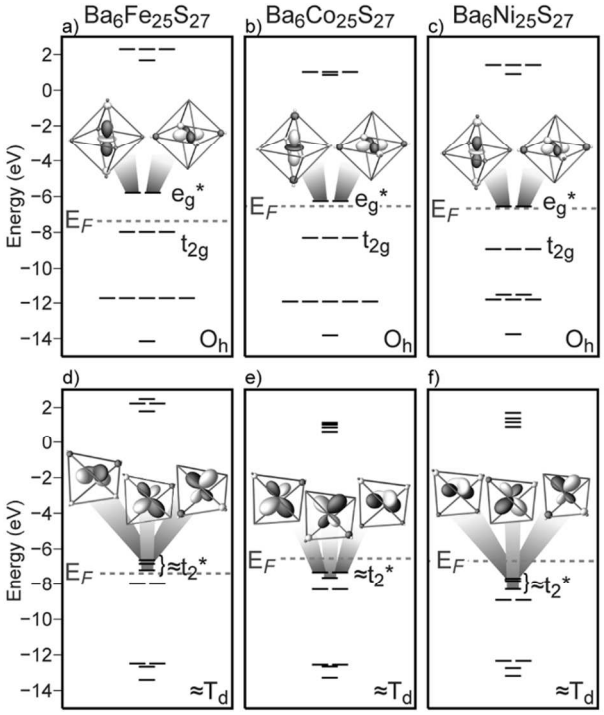

Figure 7. MO diagrams of the a-c) MS_6 and d-f) MS_4 units within $Ba_6Fe_{25}S_{27}$, $Ba_6Co_{25}S_{27}$, and $Ba_6Ni_{25}S_{27}$. The corresponding $Ba_6M_{25}S_{27}$ Fermi level is derived from an extended solid DFT-calibrated Hückel calculation and superimposed within each MO diagram. Selected spatial distributions of valence MOs are additionally plotted.

$Ba_6Fe_{25}S_{27}$ FeS_4 cluster now possesses solely occupied bonding and nonbonding orbitals. Having a set of degenerate nonbonding orbitals aligned with the Fermi energy promotes the Fe-based compound a candidate for magnetic phenomena, as we will explore later.

THE EFFECT OF BA ON COVALENT M-S INTERACTIONS: By looking at the electron density map of $Ba_6Fe_{25}S_{27}$, we inferred that Ba does not have strong covalent interactions with the nearby S atoms. Instead, the presence of the large Ba cation has an indirect influence on the covalent M-S bonding, which is observable through the change in Hückel parameters between the pentlandite and 6:25:27 phases. Because of its highly electropositive nature, Ba may have a strong influence on how S atoms bond. In Table IV, we list the parameters used to model the S p-orbital in the pentlandite phases and the 6:25:27 phases.

As mentioned before, two parameters govern the orbitals used for our DFT-calibrated Hückel model, H_{ii} (ionization potential) and ζ (diffuseness of the orbital). By looking at the parameter sets, a pattern emerges. Among the pentlandite phases, the S 3p orbital has an H_{ii} that hovers around -7.5 eV. The 6:25:27 phases lower this value by 0.5 to 1 eV (Table IV). For comparison, the S 3p parameter set for the NaCl-type BaS is provided. This phase produces an even lower H_{ii}

Dalton Transactions Accepted Manuscript

of -8.856 eV. This trend suggests that Ba induces an electrostatic stabilization of electrons from S atoms that lowers the H_{ii} of the orbital. Because these parameters are generated from a fit to an extended solid band structure calculation, the effect is not explicitly from local interactions.

In the fourth column of Table IV, we provide the H_{ii} difference between the M 3d and the S 3p orbitals—the two valence orbitals expected to yield the strongest interaction closest to the Fermi level. The pentlandite phases have a large difference, in excess of 1 eV, whereas the $Ba_6M_{25}S_{27}$ phases minimize this difference. By having Ba present, the energy of the S p orbital is lowered, and the difference in energy of interacting metal d and ligand p orbitals is reduced. This reduction causes a greater amount of dispersion in the resulting molecular orbital energy levels, spreading the distance between bonding and antibonding states. Thus, the Ba cations promote the stability of the clusters found in the pentlandite structure.

Table IV. DFT-calbrated Hückel parameters for S 3p orbitals within M_9S_8 and $Ba_6M_{25}S_{27}$ phases, and BaS. The difference in H_{ii} between the M 3d and S 3p orbitals used to model the given compound is also reported.

phase	H_{ii} (eV)	ζ	$\Delta H_{ii} = \lvert TM\ 3d - S\ 3p \rvert$
Fe_9S_8	-7.540	1.914	1.161
Co_9S_8	-7.559	2.111	1.045
Ni_9S_8	-7.451	1.987	1.442
$Ba_6Fe_{25}S_{27}$	-8.491	1.897	0.513
$Ba_6Co_{25}S_{27}$	-8.053	2.024	0.250
$Ba_6Ni_{25}S_{27}$	-8.120	1.956	0.804
BaS	-8.856	2.207	

Magnetization measurements of $Ba_6Fe_{25}S_{27}$

To evaluate the effect of magnetism on the bonding of our newly synthesized $Ba_6Fe_{25}S_{27}$ compound, we turn to magnetization measurements and use of spin-polarized density functional theory. The magnetization measurements revealed a peak at approximately 25 K, likely corresponding to an antiferromagnetic transition. Figure 8 shows zero-field cooled (ZFC) and field cooled (FC) curves for the molar magnetic susceptibility of $Ba_6Fe_{25}S_{27}$. The two curves do not necessarily trace each other below the Néel transition T_N indicating either some small spin glassy component to the antiferromagnetic ordering or the inclusion of an impurity in the crystals. The small Curie tail of the FC curve at low temperatures reflects the possibility for either one. More interestingly, above T_N, the system does not adhere to Curie paramagnetic behavior. Instead of further decreasing with temperature, the magnetic susceptibility increases above ~ 110 K until the limit of the SQUID measurement of 300 K.

Between 45 K and 85 K, a Curie-Weiss fit was performed on the inverse magnetic susceptibility (Fig. 8 inset). A large Weiss field of -238.2 K was obtained with an effective moment of 2.63 μ_B, indicating strong antiferromagnetic coupling between the Fe centers with S=1. Since the ordering temperature is much lower than the Weiss field, this would indicate that there is some form of frustration in the magnetic interactions depressing the actual Néel temperature. However, one must exercise caution in over interpreting the Curie-Weiss fit since the sample shows complex magnetic behavior above 110 K, and it is difficult to know when the system is purely in the Curie paramagnetic regime.

Comparison to the isostructural $Ba_6Ni_{25}S_{27}$ might reveal some clues. Interestingly, Gelabert et al. also noted an increase in the magnetic susceptibility of $Ba_6Ni_{25}S_{27}$ with temperature.[46] From 2K up to 225 K, the compound displays conventional Curie paramagnetism, but from 225 K up to 900 K, χ_{mol} increases. This anomaly in χ_{mol} at 225 K is also paralleled in the thermal expansion of the lattice constant and in the electrical resistivity data. Since no crystallographic phase transition of $Ba_6Ni_{25}S_{27}$ is observed, this anomalous behavior may be due to an electronic transition. $Ba_6Co_{25}S_{27}$, however, was found to be metallic and a simple Pauli paramagnet with a Curie tail, due to either an impurity or a local moment on the Co octahedral site.[45]

The rise of χ_{mol} with increasing temperature has recently been found in the Fe-based superconductor parent families, including pnictide and chalcogenide phases such as AFe_2As_2 (A=Ba, Sr, Ca), LaFeAsO, and $K_{0.8}Fe_{1.6}Se_2$.[19, 83-85] These Fe phases are also found to be long-range antiferromagnets at lower temperatures, but the susceptibility increases above T_N, all the way up to 700 K for the case of $BaFe_2As_2$.[86] These compounds are metallic and the long-ranged magnetic ordering is thought to arise from collective electron behavior instead of localized d-electrons as in insulating or semiconducting iron oxides. This anomalous behavior, also observed in the parent phases of the high-T_c cuprates, has

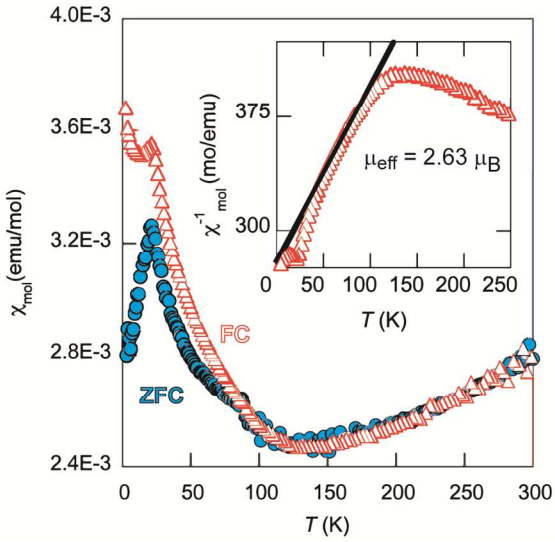

Figure 8. The molar magnetic susceptibility per iron cation in $Ba_6Fe_{25}S_{27}$ with the zero field-cooled (ZFC) measurement in blue filled circles and field cooled (ZFC) in open orange triangles. The applied field was 1000 Oe. (inset) A Curie-Weiss fit to the inverse susceptibility was attempted for a narrow temperature range of 45 K to 85 K affording an effective moment close to that of an S=1 system.

Dalton Transactions Accepted Manuscript

been attributed to strong antiferromagnetic correlations that persist up to high temperatures. Since antiferromagnetic coupling decreases overall magnetization, the increasing thermal energy acts to break this coupling, thereby increasing χ_{mol}.[84] Our spin-polarized DFT calculations shed more light as to the origins of antiferromagnetic behavior in $Ba_6Fe_{25}S_{27}$.

Magnetism's influence on bonding in $Ba_6Fe_{25}S_{27}$: To determine the effect of magnetism on the electronic structure of $Ba_6Fe_{25}S_{27}$, we performed spin-polarized DFT calculations for different magnetic alignments of the Fe centers and compared their total energies to the result from the nonmagnetic phase. Three magnetic orderings for the $Ba_6Fe_{25}S_{27}$ structure were considered: ferromagnetic (FM) alignment, antiferromagnetic (AFM) alignment of the tetrahedral iron sites, and AFM alignment with a magnetic moment on the octahedral iron site. For AFM alignment, only the A-type alignment was considered. This configuration calls for ferromagnetic coupling between iron centers with close Fe-Fe distances (~2.72 Å) and antiferromagnetic coupling between the iron centers with the longer distance (~2.78 Å). Although only one of many AFM alignments was modeled, the results still provide insight into how the $Ba_6Fe_{25}S_{27}$ electronic structure reacts to adopting a magnetic state. The total energy results of these calculations are reported in Table V.

Table V. Total energy values of $Ba_6M_{25}S_{27}$ phases, determined from nonmagnetic and spin polarized DFT calculations.

phase	Spin alignment	Total energy (eV)
$Ba_6Fe_{25}S_{27}$	nonmagnetic	-230.32
	FM	-292.65
	AFM	-295.84
	AFM + O_h	-296.56
$Ba_6Co_{25}S_{27}$	nonmagnetic	-233.73
	AFM	-241.44
$Ba_6Ni_{25}S_{27}$	nonmagnetic	-229.20
	AFM	-226.58

Compared to the nonmagnetic state, there is a large stabilization of 62.33 eV from $Ba_6Fe_{25}S_{27}$ adopting a spin-polarized state, moving from -230.32 to -292.65 eV (Table V). Within the spin polarized calculations, the AFM spin state is favored over the FM state by 3.91 eV, and placing a magnetic moment on the octahedral iron site lowers the energy slightly further by less than 1 eV. The average calculated magnetic moment of the Fe centers in the AFM configuration is 3.2 μ_B, implying an intermediate spin state of S=3/2.

Additionally reported in Table VII are total energies from calculations on the nonmagnetic and magnetic structures of $Ba_6Co_{25}S_{27}$ and $Ba_6Ni_{25}S_{27}$. $Ba_6Co_{25}S_{27}$ is stabilized by less than one sixth the amount of the Fe-based phase, reducing its total energy by 7.71 eV. It is also worth noting that while the Fe based phase easily converges on an AFM-ordering with equally opposing magnetic moments, the Co based phase converges on an uncompensated ferrimagnetic structure. $Ba_6Ni_{25}S_{27}$ experiences a destabilizing effect from adopting an antiferromagnetic spin state, converging on a magnetic alignment that has a very small moment on each Ni atom.

The calculated results complement the existing magnetic data, both from our experimental measurements on $Ba_6Fe_{25}S_{27}$ and those performed by Glaubert and DiSalvo on $Ba_6Co_{25}S_{27}$ and $Ba_6Ni_{25}S_{27}$. In previous studies, both $Ba_6Co_{25}S_{27}$ and $Ba_6Ni_{25}S_{27}$ did not elicit a magnetic response to indicate a preferred antiferromagnetic alignment. Within our measurements of the Fe-based phase, however, we showed a distinct response at 25K, which is indicative of an antiferromagnetic transition. Although the experimentally observed magnetic moment for the Fe centers is slightly lower than our computational result, the consistency between the experimental and computational result encourages our continued analysis.

The DOS distribution of the spin-polarized $Ba_6Fe_{25}S_{27}$ calculation provides clues as to why this phase is prone to adopting an AFM configuration. In Figure 9a, the DOS distribution of the nonmagnetic structure of $Ba_6Fe_{25}S_{27}$ is plotted. To follow our MO based analysis, we additionally plot the projection of the *e* and t_2 orbitals for the tetrahedral Fe sites (marked in red and blue, respectively). Within the nonmagnetic DOS distribution, the Fermi energy resides in the middle of a large hump in the distribution at around 7 eV, and a large peak of states sits directly below the Fermi energy. Based on our previous assessment with our MO model, the large peak can be linked to nonbonding interactions, both from the tetrahedral and octahedral iron clusters. The additional block of states from -10 to -13 eV can be correlated to the low lying bonding states from the tetrahedral cluster. The pDOS of the t_2 states begin to form some type of pseudogap around the Fermi energy. Within the *e* pDOS, however, this gap is less apparent, appearing more as a broadened distribution of states through the Fermi level.

When spin polarization is incorporated, the distribution changes signficantly. Figure 9b depicts the DOS distribution of $Ba_6Fe_{25}S_{27}$ when it adopts an AFM spin arrangement. Now a large pseudogap in the DOS distribution opens up, and the Fermi energy sits exactly inside the gap. The *e* pDOS reorganizes such that the large peak below the Fermi energy in the nonmagnetic distribution disappears. These states instead form a peak above and a broad distribution of states below the Fermi energy. Additionally, the t_2 states widen the pseudogap around the Fermi energy.

We decompose the Fe d states in an alternate way in Figure 9c to elucidate the mechanism behind this magnetic reorganization of states. The DOS distribution now exhibits two sets of d states—spin majority d-states in which the spin is aligned with the magnetic moment (spin-up on a spin-up site), and spin minority states which oppose that alignment (spin-up on a spin-down site). The spin majority Fe d pDOS, plotted in blue, is aggregated almost entirely below the Fermi energy.

Dalton Transactions Accepted Manuscript

The spin minority Fe d pDOS, however, straddles the pseudogap, locating states above and below the Fermi energy. The difference in the spin majority and spin minority

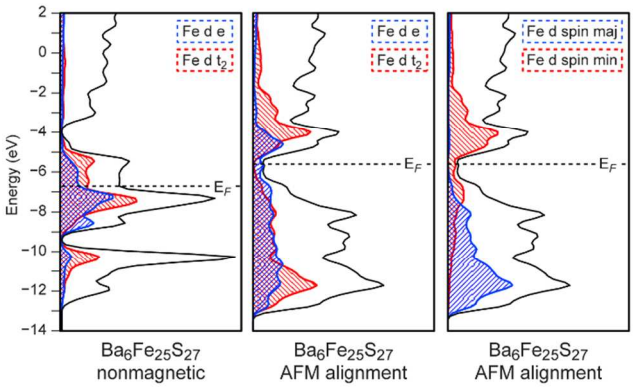

Figure 9. Calculated DOS distributions of the a) $Ba_6Fe_{25}S_{27}$ nonmagnetic and b-c) antiferromagnetic configurations. Within a) and b), pDOS of the *e* and t_2 d-states for the tetrahedrally coordinated Fe atoms are provided. The third DOS in c) shows projected Fe d states from sites with spin up majority and spin-up minority. Figure 9b-c only show the up-spin states as the down-spin states have a near identical distribution.

pDOS can be explained from the perspective of the exchange hole: the majority spin electrons should experience less shielding from the nucleus and aggregate around lower energy values, while minority spin electrons experience the opposite effect.[87, 88] By adopting an AFM arrangement, the polarization of the Fe spin majority and spin minority states are highly differentiated, leading to a new source of stability within the electronic structure.

Conclusions

Within this article, we have detailed the synthesis of a new ternary compound $Ba_6Fe_{25}S_{27}$, which crystallizes in the djerfisherite structure type. By adding Ba to Fe and S, fragments of the Co_9S_8-type structure can be stabilized, permitting a new three dimensional clustering of FeS_4 tetrahedra among ternary phases. From magnetic measurements, we have determined that $Ba_6Fe_{25}S_{27}$ exhibits an antiferromagnetic ordering transition at 25 K, along with anomalous high-temperature behavior that is distinctively not Curie-like. Although hints of antiferromagnetism have been previously observed in octonuclear complexes, the strength of the magnetic moment in $Ba_6Fe_{25}S_{27}$ (2.63 μ_B) appears to be unprecedented among the family of octonuclear complex compounds.

Through our structural exploration of solid state compounds that contain the rhombohedral $M_8(\mu_4\text{-}X)_6Y_8$ cluster, we isolated two specific coordinating units—the MS_4 tetrahedron and MS_6 octahedron. Using DFT-calibrated Hückel theory, we developed a molecular orbital based model of these units. This simplified model yielded a concise explanation of the connection between stability of the pentlandite phase and its constituent clusters. The Co_9S_8 phase possesses an electron count which satisfies both the 18 electron rule for its octahedral and tetrahedral Co-S fragments. Lowering this electron count destabilizes the tetrahedral electronic structure, and increasing the electron count destabilizes the MS_6 unit, thereby making Fe_9S_8 and Ni_9S_8 unstable and unobserved phases.

By adding Ba to the pentlandite phase, the sensitivity of the phase to electron count is lowered—both the Fe and Ni based phases form. In the case of the Ni analog, antibonding levels are moved above the Fermi level, causing them to become depopulated. The Fe analog also moves states with antibonding character above the Fermi energy. In the Fe case, the tetrahedral 18 electron rule is disrupted to populate states with strictly nonbonding character at the HOMO. Ba is able to promote this shift in energy levels by lowering the ionization energy of the S ligands in the compound, which in turn diminishes the energy difference between Fe d and S p orbitals and enhances their covalency in bonding.

By leaving nonbonding energy levels at the Fermi energy, $Ba_6Fe_{25}S_{27}$ is uniquely susceptible to adopting a magnetic state, further driving the stability of the phase. The spin polarization created by the magnetic ordering of $Ba_6Fe_{25}S_{27}$ is seen to stabilize the structure from a quantitative, total energy perspective. This stability is also visible from a more qualitative level with the DOS distribution: a pseudogap opens around the Fermi energy upon allowing the nonbonding states to polarize.

In light of the discovery of superconductivity in metallic Fe (II) pnictides by Hosono *et al.* in 2006,[21] and more recently in Fe (II) chalcogenide phases by several groups,[31—33] we have pursued the synthesis of novel metallic iron sulfides. While the mechanism behind superconductivity remains unknown, it is generally understood that magnetism is implicated. The question of why only the iron compounds exhibit unconventional superconductivity while the cobalt and nickel analogues do not may be related to the special d^6 electron configuration of the Fe(II) tetrahedral species and the magnetic coupling arising from Hund's rules. Since the $Ba_6Fe_{25}S_{27}$ phase contains low-valent Fe centers in tetrahedral arrangements, it will provide us with a testing bed for properties similar to the Fe-based superconductors. Furthermore, the interesting temperature dependence of the magnetization is similar to that of the parent phases of superconductors such as $BaFe_2As_2$ and LaOFeAs. Thus, electron and hold-doping experiments of $Ba_6Fe_{25}S_{27}$ will be imperative to understanding the role of magnetism on the electronic properties of these novel materials.

Acknowledgements

We thank the University of Maryland-College Park for funding the research for this project. We also thank Pouya Moetakef for assistance in the magnetic measurements, and Danny Fredrickson, Brandon Kilduff, and Vincent Yannello for their helpful insight into development of the DFT-Hückel MO models.

References

Dalton Transactions Accepted Manuscript

1. R. H. Holm, P. Kennepohl and E. I. Solomon, *Chem. Rev.*, 1996, **96**, 2239-2314.
2. H. Beinert, R. H. Holm and E. Munck, *Science*, 1997, **277**, 653-659.
3. D. Coucouvanis and M. G. Kanatzidis, *J. Am. Chem. Soc.*, 1985, **107**, 5005-5006.
4. M. G. Kanatzidis, W. R. Hagen, W. R. Dunham, R. K. Lester and D. Coucouvanis, *J. Am. Chem. Soc.*, 1985, **107**, 953-961.
5. D. Coucouvanis, A. Salifoglou, M. G. Kanatzidis, W. R. Dunham, A. Simopoulos and A. Kostikas, *Inorg. Chem.*, 1988, **27**, 4066-4077.
6. S. Pohl and U. Opitz, *Angew. Chem. Int. Edit.*, 1993, **32**, 863-864.
7. C. Junghans, W. Saak and S. Pohl, *J. Chem. Soc. Chem. Comm.*, 1994, 2327-2328.
8. J. R. Long and R. H. Holm, *J. Am. Chem. Soc.*, 1994, **116**, 9987-10002.
9. L. D. Lower and L. F. Dahl, *J. Am. Chem. Soc.*, 1976, **98**, 5046-5047.
10. D. Fenske, R. Basoglu, J. Hachgenei and F. Rogel, *Angew. Chem. Int. Edit.*, 1984, **23**, 160-162.
11. D. Fenske, J. Hachgenei and J. Ohmer, *Angew. Chem. Int. Edit.*, 1985, **24**, 706-709.
12. D. Fenske, J. Ohmer, J. Hachgenei and K. Merzweiler, *Angew. Chem. Int. Edit.*, 1988, **27**, 1277-1296.
13. G. Christou, K. S. Hagen and R. H. Holm, *J. Am. Chem. Soc.*, 1982, **104**, 1744-1745.
14. G. Christou, K. S. Hagen, J. K. Bashkin and R. H. Holm, *Inorg. Chem.*, 1985, **24**, 1010-1018.
15. S. Pohl and W. Saak, *Angew. Chem. Int. Edit.*, 1984, **23**, 907-908.
16. W. Saak and S. Pohl, *Angew. Chem. Int. Edit.*, 1991, **30**, 881-883.
17. S. Pohl, W. Barklage, W. Saak and U. Opitz, *J. Chem. Soc. Chem. Comm.*, 1993, 1251-1252.
18. A. D. Pearson and M. J. Buerger, *Am. Mineral.*, 1956, **41**, 804-805.
19. J. Paglione and R. L. Greene, *Nat. Phys.*, 2010, **6**, 645-658.
20. Y. Kamihara, H. Hiramatsu, M. Hirano, R. Kawamura, H. Yanagi, T. Kamiya and H. Hosono, *J. Amer. Chem. Soc.*, 2006, **128**, 10012-10013.
21. Y. Kamihara, T. Watanabe, M. Hirano and H. Hosono, *J. Am. Chem. Soc.*, 2008, **130**, 3296-3297.
22. X. H. Chen, T. Wu, G. Wu, R. H. Liu, H. Chen and D. F. Fang, *Nature*, 2008, **453**, 761-762.
23. C. de la Cruz, Q. Huang, J. W. Lynn, J. Li, W. Ratcliff, II, J. L. Zarestky, H. A. Mook, G. F. Chen, J. L. Luo, N. L. Wang and P. Dai, *Nature*, 2008, **453**, 899-902.
24. T. J. Liu, J. Hu, B. Qian, D. Fobes, Z. Q. Mao, W. Bao, M. Reehuis, S. A. J. Kimber, K. Prokes, S. Matas, D. N. Argyriou, A. Hiess, A. Rotaru, H. Pham, L. Spinu, Y. Qiu, V. Thampy, A. T. Savici, J. A. Rodriguez and C. Broholm, *Nat. Mater.*, 2010, **9**, 716-720.
25. S. Medvedev, T. M. McQueen, I. A. Troyan, T. Palasyuk, M. I. Eremets, R. J. Cava, S. Naghavi, F. Casper, V. Ksenofontov, G. Wortmann and C. Felser, *Nat. Mater.*, 2009, **8**, 630-633.
26. P. Zajdel, P.-Y. Hsieh, E. E. Rodriguez, N. P. Butch, J. D. Magill, J. Paglione, P. Zavalij, M. R. Suchomel and M. A. Green, *J. Am. Chem. Soc.*, 2010, **132**, 13000-13007.
27. D. R. Parker, M. J. Pitcher, P. J. Baker, I. Franke, T. Lancaster, S. J. Blundell and S. J. Clarke, *Chem. Comm.*, 2009, 2189-2191.
28. D. R. Parker, M. J. P. Smith, T. Lancaster, A. J. Steele, I. Franke, P. J. Baker, F. L. Pratt, M. J. Pitcher, S. J. Blundell and S. J. Clarke, *Phys. Rev. Lett.*, 2010, **104**, 057007.
29. D. Mandrus, A. S. Sefat, M. A. McGuire and B. C. Sales, *Chem. Mater.*, 2010, **22**, 715-723.
30. Y. Mizuguchi and Y. Takano, *J. Phys. Soc. Jpn.*, 2010, **79**.
31. T. Ying, X. Chen, G. Wang, S. Jin, X. Lai, T. Zhou, H. Zhang, S. Shen and W. Wang, *J. Am. Chem. Soc.*, 2013, **135**, 2951-2954.
32. M. Burrard-Lucas, D. G. Free, S. J. Sedlmaier, J. D. Wright, S. J. Cassidy, Y. Hara, A. J. Corkett, T. Lancaster, P. J. Baker, S. J. Blundell and S. J. Clarke, *Nat. Mater.*, 2013, **12**, 15-19.
33. S. J. Sedlmaier, S. J. Cassidy, R. G. Morris, M. Drakopoulos, C. Reinhard, S. J. Moorhouse, D. O'Hare, P. Manuel, D. Khalyavin and S. J. Clarke, *J. Am. Chem. Soc.*, 2014, **136**, 630-633.
34. O. Fischer, *Appl. Phys.*, 1978, **16**, 1-28.
35. R. Chevrel, M. Sergent and J. Prigent, *J. Solid State Chem.*, 1971, **3**, 515-519.
36. J. R. Long, L. S. McCarty and R. H. Holm, *J. Am. Chem. Soc.*, 1996, **118**, 4603-4616.
37. L. G. Beauvais, M. P. Shores and J. R. Long, *Chem. Mater.*, 1998, **10**, 3783-3786.
38. J. D. Corbett, *J. Solid State Chem.*, 1981, **39**, 56-74.
39. T. Saito, N. Yamamoto, T. Nagase, T. Tsuboi, K. Kobayashi, T. Yamagata, H. Imoto and K. Unoura, *Inorg. Chem.*, 1990, **29**, 764-770.
40. J. T. Lemley, J. M. Jenks, J. T. Hoggins, Z. Eliezer and H. Steinfink, *J. Solid State Chem.*, 1976, **16**, 117-128.
41. J. T. Hoggins and H. Steinfink, *Acta Cryst. B*, 1977, **33**, 673-678.
42. J. T. Hoggins, L. E. Rendondiazmiron and H. Steinfink, *J. Solid State Chem.*, 1977, **21**, 79-90.
43. I. E. Grey, H. Hong and H. Steinfin, *Inorg. Chem.*, 1971, **10**, 340-343.
44. H. Y. Hong and H. Steinfin, *J. Solid State Chem.*, 1972, **5**, 93-104.
45. G. J. Snyder, M. E. Badding and F. J. Disalvo, *Inorg. Chem.*, 1992, **31**, 2107-2110.
46. M. C. Gelabert, M. H. Ho, A. S. Malik, F. J. DiSalvo, P. Deniard and R. Brec, *Chem.-Eur. J.*, 1997, **3**, 1884-1889.
47. Bruker, *Apex2*, Bruker AXS Inc., Madison, Wisconsin, USA, 2010.
48. G. M. Sheldrick, *Acta Cryst. A*, 2008, **64**, 112-122.
49. J. P. Perdew, J. A. Chevary, S. H. Vosko, K. A. Jackson, M. R. Pederson, D. J. Singh and C. Fiolhais, *Phys. Rev. B*, 1992, **46**, 6671-6687.
50. G. Kresse and J. Hafner, *Phys. Rev. B*, 1993, **47**, 558-561.
51. G. Kresse and J. Hafner, *Phys. Rev. B*, 1994, **49**, 14251-14269.
52. G. Kresse and J. Furthmuller, *Comput. Mater. Sci.*, 1996, **6**, 15–50.

Dalton Transactions Accepted Manuscript

53. G. Kresse and J. Furthmuller, *Phys. Rev. B*, 1996, **54**, 11169-11186.
54. P. E. Blochl, *Phys. Rev. B*, 1994, **50**, 17953-17979.
55. G. Kresse and D. Joubert, *Phys. Rev. B*, 1999, **59**, 1758-1775.
56. A. Stroppa and G. Kresse, *Phys. Rev. B*, 2009, **79**, 201201.
57. S. Dudarev, G. A. Botton, S. Y. Savrasov, C. J. Humphreys and A. P. Sutton, *Phys. Rev. B*, 1998, **57**, 1505-1509.
58. E. Hückel, *Z. Phys.*, 1931, **70**, 204-286.
59. E. Hückel, *Z. Phys.*, 1931, **72**, 310–337.
60. E. Hückel, *Z. Phys.*, 1932, **76**, 628–648.
61. E. Hückel, *Z. Phys.*, 1933, **83**, 632–668.
62. G. A. Landrum, *YAeHMOP: Yet Another extended Hückel Molecular Orbital Package, Version 3.0*; YAeHMOP is freely available on the WWW at URL: http://sourceforge.net/projects/yaehmop/.
63. M. Wolfsberg and L. Helmholz, *J. Chem. Phys.*, 1952, **20**, 837-843.
64. J. H. Ammeter, H. B. Burgi, J. C. Thibeault and R. Hoffmann, *J. Am. Chem. Soc.*, 1978, **100**, 3686-3692.
65. T. E. Stacey and D. C. Fredrickson, *Dalton T.*, 2012, **41**, 7801-7813.
66. L. H. Fuchs, *Science*, 1966, **153**, 166-167.
67. H. T. Evans and J. R. Clark, *Am. Mineral.*, 1981, **66**, 376-384.
68. K. Kim, *B. Kor. Chem. Soc.*, 1986, **7**, 102-105.
69. O. Knop, C. H. Huang, K. I. G. Reid, J. S. Carlow and F. W. D. Woodhams, *J. Solid State Chem.*, 1976, **16**, 97-116.
70. E. Furet, A. Lebeuze, J. F. Halet and J. Y. Saillard, *J. Am. Chem. Soc.*, 1994, **116**, 274-280.
71. J. K. Burdett and G. J. Miller, *J. Am. Chem. Soc.*, 1987, **109**, 4081-4091.
72. G. G. Hoffman, J. K. Bashkin and M. Karplus, *J. Am. Chem. Soc.*, 1990, **112**, 8705-8714.
73. D. N.-M. H. R. Chauke, P. E. Ngoepe, D. G. Pettifor, and S. G. Fries, *Phys. Rev. B*, 2014, **66**, 155105.
74. J. K. Burdett, *Molecular Shapes: Theoretical Models of Inorganic Stereochemistry*, John Wiley & Sons Inc, 1980.
75. S. Lee, *Annu. Rev. Phys. Chem.*, 1996, **47**, 397-419.
76. R. Hoffmann, *Solids and Surfaces: A Chemist's View of Bonding in Extended Structures*, Wiley-VCH, 1989.
77. J. K. Burdett, *Chemical Bonding in Solids (Topics in Inorganic Chemistry)*, Oxford University Press, USA, 1995.
78. R. T. Fredrickson and D. C. Fredrickson, *Inorg. Chem.*, 2012, **51**, 10341-10349.
79. R. T. Fredrickson and D. C. Fredrickson, *Inorg. Chem.*, 2013, **52**, 3178-3189.
80. D. Fredrickson, I. Doverbratt, S. Ponou and S. Lidin, *Crystals*, 2013, **3**, 504-516.
81. R. Dronskowski and P. E. Blochl, *J. Phys. Chem.*, 1993, **97**, 8617-8624.
82. P. Atkins, *Shriver & Atkins' Inorganic Chemistry*, Oxford University Press, 2010.
83. X.-W. Yan, M. Gao, Z.-Y. Lu and T. Xiang, *Phys. Rev. B*, 2011, **83**, 233205.
84. D. C. Johnston, *Adv. Phys.*, 2010, **59**, 803-1061.
85. R. Klingeler, N. Leps, I. Hellmann, A. Popa, U. Stockert, C. Hess, V. Kataev, H. J. Grafe, F. Hammerath, G. Lang, S. Wurmehl, G. Behr, L. Harnagea, S. Singh and B. Buchner, *Phys. Rev. B*, 2010, **81**, 024506.
86. X. F. Wang, T. Wu, G. Wu, R. H. Liu, H. Chen, Y. L. Xie and X. H. Chen, *New J. Phys.*, 2009, **11**, 11.
87. G. A. Landrum and R. Dronskowski, *Angew. Chem. Int. Edit.*, 2000, **39**, 1560-1585.
88. A. Decker, G. A. Landrum and R. Dronskowski, *Z. Anorg. Chem.*, 2002, **628**, 303-309.

Dalton Transactions Accepted Manuscript

Dalton Transactions Accepted Manuscript

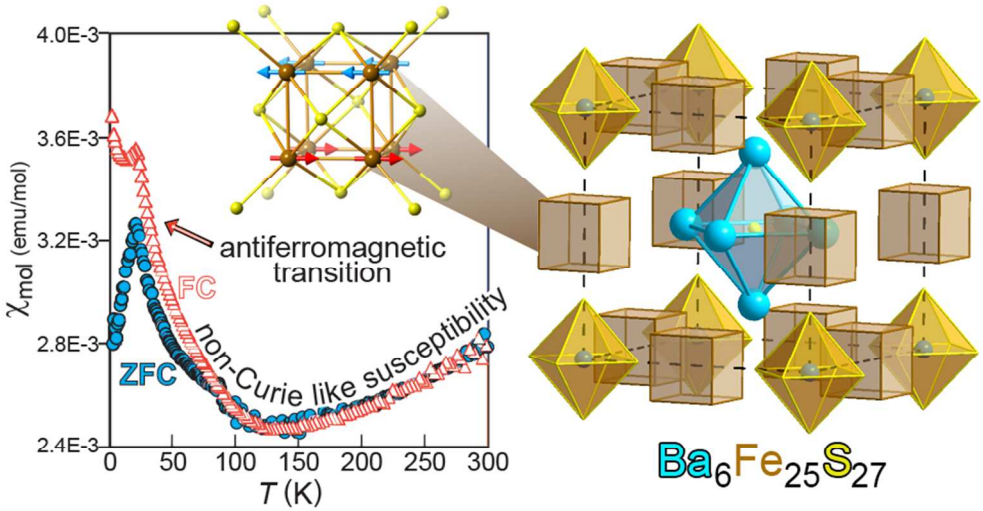

82x44mm (300 x 300 DPI)

Dalton Transactions Accepted Manuscript